

Revisiting Monocular 3D Object Detection with Depth Thickness Field

Qiude Zhang, Chunyu Lin*, Zhijie Shen, Nie Lang, and Yao Zhao

Institute of Information Science, Beijing Jiaotong University

Beijing Key Laboratory of Advanced Information Science and Network Technology

{zhangqiude, cylin}@bjtu.edu.cn

Abstract

Monocular 3D object detection is challenging due to the lack of accurate depth. However, existing depth-assisted solutions still exhibit inferior performance, whose reason is universally acknowledged as the unsatisfactory accuracy of monocular depth estimation models. In this paper, we revisit monocular 3D object detection from the depth perspective and formulate an additional issue as the limited 3D structure-aware capability of existing depth representations (e.g., depth one-hot encoding or depth distribution). To address this issue, we introduce a novel **Depth Thickness Field** approach to embed clear 3D structures of the scenes. Specifically, we present **MonoDTF**, a scene-to-instance depth-adapted network for monocular 3D object detection. The framework mainly comprises a Scene-Level Depth Retargeting (SDR) module and an Instance-Level Spatial Refinement (ISR) module. The former retargets traditional depth representations to the proposed depth thickness field, incorporating the scene-level perception of 3D structures. The latter refines the voxel space with the guidance of instances, enhancing the 3D instance-aware capability of the depth thickness field and thus improving detection accuracy. Extensive experiments on the KITTI and Waymo datasets demonstrate our superiority to existing state-of-the-art (SoTA) methods and the universality when equipped with different depth estimation models. The code will be available.

1. Introduction

3D object detection is critical in computer vision and has a wide range of applications, such as autonomous driving, robotic perception, etc. Although the methods based on LiDAR [16, 35, 44] and multi-view images [9, 17, 19, 31] have achieved promising performance, the heavy dependence on the expensive equipment [4, 26] restricts the application of these methods. Recently, there have been consid-

*Corresponding author.

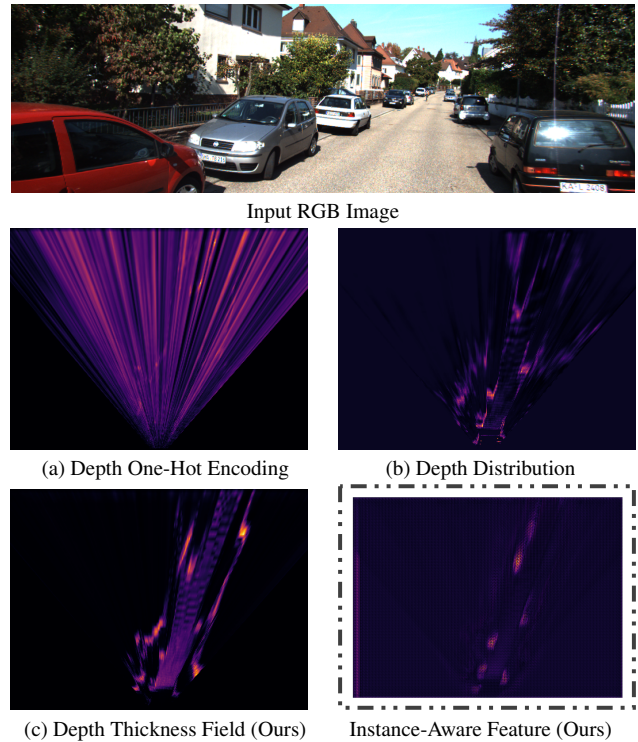


Figure 1. (a), (b), and (c) show VOXEL features from three different depth representations. (c) provides a more comprehensive and clearer scene structure feature. The last image surrounded by a dashed box represents instance-aware BEV features derived from (c), focusing on instance structure.

erable advancements in monocular methods [21, 23, 29, 30, 42] and garnered substantial attention from both academic and industrial communities, which give credit to their low cost and ease of deployment.

Monocular 3D object detection can be directly assisted by monocular depth estimation. However, inferring depth from a monocular image is inherently an ill-posed problem that affects the performance of monocular 3D object detection. Early depth-assisted methods [5, 40] resort to pre-training an auxiliary depth estimator, e.g., MonoDepth2

[8], to predict depth maps, but cannot achieve satisfactory detection performance. Most solutions (e.g., DD3D [27]) attribute it to the limited accuracy of monocular depth estimation models while overlooking the significance of depth representations. Recently, benefiting from the large-scale dataset and self-supervised training strategy, monocular depth estimation using large models (e.g., Depth Anything V2 (DAM v2) [45] and Metric3D v2 [46]) exhibit impressive accuracy and generalization. An intuitive idea is to leverage them to improve monocular 3D object detection. Unfortunately, as reported in Sec. 4.4, the results remain unsatisfactory, which drives us to rethink the well-recognized issue (i.e., limited depth accuracy problem) and revisit this type of approaches. In this work, we hold a different idea and contend that this issue also stems from the limited 3D structure awareness of existing depth representations (e.g., depth one-hot encoding or depth distribution).

To address this issue, we propose MonoDTF, a novel scene-to-instance depth-adapted monocular 3D detection network. Different from existing approaches [30, 33] that adapt Lift-Splat-Shoot (LSS) [31] framework and bird’s-eye-view (BEV) space, MonoDTF retargets traditional depth representations in a new formulation: **Depth Thickness Field (DTF)** to adapt to 3D object detection. The DTF can reduce the impact of erroneous depth estimation and integrate the thickness property for each image pixel in the 3D space. It implicitly describes the thickness along camera rays, producing sharper and more accurate features, as illustrated in Fig. 1. MonoDTF consists of two main components. First of all, a Scene-Level Depth Retargeting (SDR) module is presented to retarget traditional depth representations to the proposed depth thickness field. Compared with previous representations, the DTF embeds clear 3D structure awareness, benefiting in distinguishing different instances and backgrounds. Then, we sample image features and depth thickness field to establish the voxel space with predefined grids. Second, an Instance-Level Spatial Refinement (ISR) module is proposed to refine the voxel space by raising the oversight of individual instances. The network can focus more on the location and volume of instances than the whole 3D scene, enhancing the 3D instance-aware capability of the proposed depth thickness field and thereby improving detection accuracy.

The main contributions are summarized as follows.

- We investigate the issue of depth-assisted methods as the limited 3D structure-aware capability of existing depth representations and present a network (termed MonoDTF) with a novel depth representation, Depth Thickness Field, to solve it.
- We design a Scene-Level Depth Retargeting (SDR) module that retargets traditional depth representations to the proposed Depth Thickness Field, incorporating the scene-level perception of 3D structures.

- To enhance the 3D instance-aware capability of the depth thickness field, an Instance-Level Spatial Refinement (ISR) module is proposed to refine the voxel space and further improve detection accuracy.
- Compared with SoTA solutions, the proposed MonoDTF demonstrates superior accuracy and generalizability.

2. Related Work

2.1. Monocular 3D Detection

In recent years, substantial progress has been made in monocular 3D detection. Nevertheless, inferring 3D information from a 2D image presents an ill-posed problem. Previous works [10, 25, 29, 33] have employed a single module for the supervised learning of dense depth maps. DD3D [27] utilizes additional extensive unlabeled data from DDAD15M for depth pre-training, resulting in substantial enhancements in the performance of monocular 3D detection. More recently, MonoCD [43] suggests leveraging the geometric relationships among various depth cues to attain complementary form enhancements. Recent progress in monocular 3D detection has incorporated instance attributes [20, 49], which helps to tackle the inherent difficulties of this ill-posed task more effectively. Our method focuses on retargeting the traditional depth representations to a new formulation: depth thickness field, thereby improving the accuracy of 3D detection.

2.2. Monocular Depth Estimation

Monocular depth estimation aims to generate a single depth value for every pixel in an image. Neural network-based methods [8, 34, 39] often regress continuous depth by aggregating color and geometric structure information from an image. However, these methods are susceptible to overfitting to a single scenario, a common issue in monocular depth estimation. Recent methods [1, 37] have effectively mitigated the problem by creating large-scale relative depth datasets to learn relative relations. DAMv2 [45] unleashes the power of large-scale unlabeled data through semantic segmentation-assisted supervision and data augmentation. Metric3Dv2 [46] introduces a canonical camera transformation to resolve metric depth ambiguity across different camera setups, significantly improving depth accuracy and generalization. In our work, we utilize the depth map generated by the depth estimation model as a depth prior for the 3D detection model, guiding the generation of the depth thickness field representation.

2.3. 3D Spatial Representations

Representing features in 3D space, such as BEV grids, removes scale differences in the targets and makes it easier for the network to learn feature scale consistency. Many works [9, 17, 19, 24, 33] employ BEV representations and

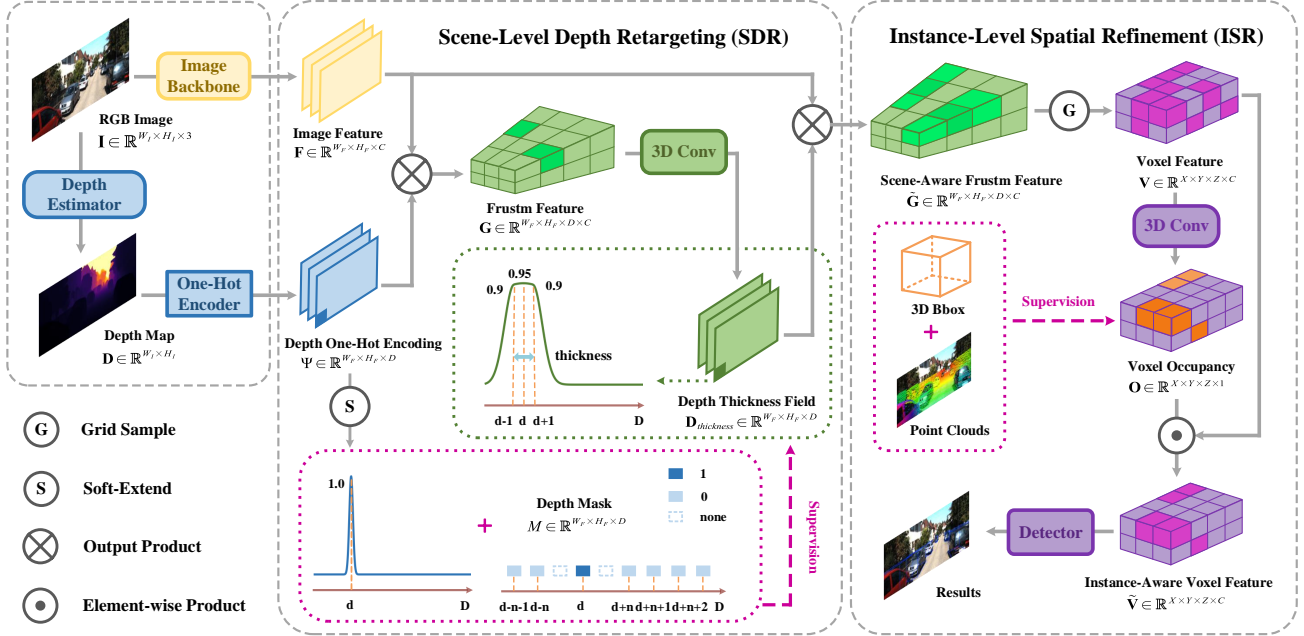


Figure 2. **The overall framework of our proposed MonoDTE.** The input image is first sent to the backbone to extract the features and the depth map is transformed to depth one-hot encoding in parallel. The Scene-Level Depth Retargeting (SDR) module implicitly learns 3D scene structure features, retargeting depth one-hot encoding to depth thickness field (Sec. 3.3). The Instance-Level Spatial Refinement (ISR) module refines the voxel features with the guidance of instances, eliminating the ambiguity of 3D occupation (Sec. 3.4). Finally, the detector is applied to predict the 3D bounding boxes.

achieve great success. LSS [31] generates point clouds by learning a pixel-level depth distribution and projecting it to obtain BEV features. BEVDepth [17] supervises the depth distribution using a projection of the depth map from the point cloud, thus improving the 3D detection performance. CaDDN [33] first used BEV representations for monocular 3D detection, and our approach follows its basic architecture design. Additionally, occupancy as an explicit representation of 3D space has recently experienced a surge in research. TPVFormer [11] employs sparse 3D occupancy labels from LiDAR as the supervision to obtain 3D features. Unlike the above methods, we concentrate on combining occupancy representation and 3D bounding box (bbox) to explore the mutual support of occupancy and monocular 3D detection tasks.

3. Methodology

3.1. Preliminary and Overview

Task Definition. Given a single RGB image, monocular 3D object detection aims to recognize objects of interest and predict their 3D attributes, including 3D location (x, y, z) , dimension (h, w, l) , and orientation θ . Existing approaches mainly focus on outdoor dynamic objects, with particular emphasis on the *Car* category [26].

Framework Overview. As illustrated in Figure 2, our

framework takes a 3-channel RGB image and a single-channel depth map (generated by a pre-trained model) as input and outputs the 3D bounding box parameters of the object in the image. Initially, the RGB image $\mathbf{I} \in \mathbb{R}^{W_I \times H_I \times 3}$ is passed through the backbone (DLA34 [47]) to extract image features, while the depth map $\mathbf{D} \in \mathbb{R}^{W_I \times H_I}$ is converted into depth one-hot encoding representation. Next, the extracted image features $\mathbf{F} \in \mathbb{R}^{W_F \times H_F \times C}$ and depth one-hot encoding $\Psi \in \mathbb{R}^{W_F \times H_F \times D}$ are fed into the SDR module for further processing. Specifically, we employ the depth one-hot encoding representation to transform the extracted features into frustum features format $\mathbf{G} \in \mathbb{R}^{W_F \times H_F \times D \times C}$. Then the depth thickness field $\mathbf{D}_{thickness} \in \mathbb{R}^{W_F \times H_F \times D}$ is adaptively learned under the supervision of our proposed soft-extended one-hot encoding. This depth thickness field is then used to refine the original image features and produce new frustum features $\tilde{\mathbf{G}} \in \mathbb{R}^{W_F \times H_F \times D \times C}$. Following this, grid sampling is applied to voxelize the 3D features. The voxel features, denoted as $\mathbf{V} \in \mathbb{R}^{X \times Y \times Z \times C}$, are subsequently fed into the ISR module. This module refines the voxel space representation by learning an occupancy map, which is guided by the enhanced occupancy labels. Finally, the refined voxel features $\tilde{\mathbf{V}} \in \mathbb{R}^{X \times Y \times Z \times C}$ are compressed into a bird’s-eye view (BEV) space and forwarded to the 3D detection head to output the results.

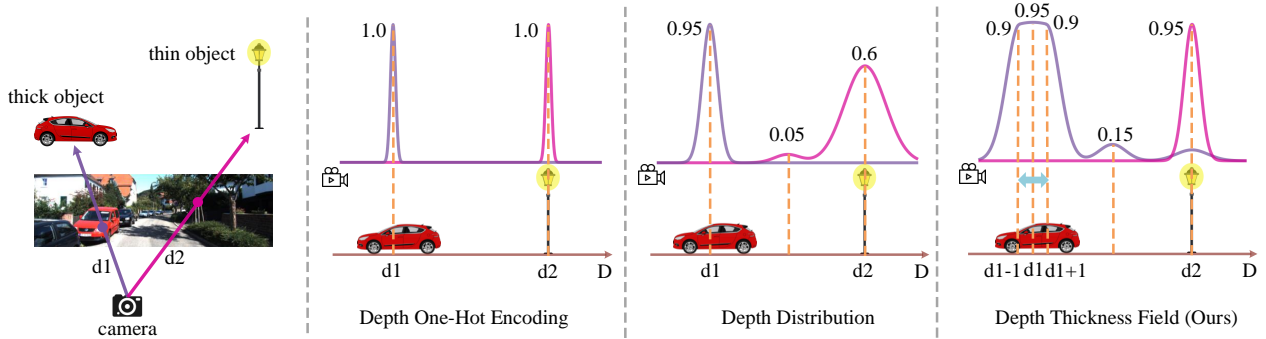


Figure 3. **Comparisons between different depth representations.** The two curves indicate the confidence of the pixel on each depth bin, obtained from three different depth representations respectively. The purple curve represents a thick object, and the pink one represents a thin object. The depth thickness field has the unique ability to represent the object thickness along the camera ray.

3.2. Depth Thickness Field

Existing 3D object detection methods [29, 43] incorporate depth information to enhance 3D perception. However, depth estimation and 3D object detection are different tasks. Inappropriate depth representations often fail to provide meaningful cues for accurate detection. In this paper, we propose a novel depth representation method, termed *Depth Thickness Field*, which is more effective for 3D object detection. To clarify our contributions, we first review two commonly used depth representation methods—depth one-hot encoding and depth distribution—before detailing our proposed approach.

Depth One-Hot Encoding. Given a pixel located at position (u, v) in a depth map, its depth value z can be converted to z' using linear-increasing discretization (LID) [38]. Then we employ D depth bins to represent the corresponding depth one-hot encoding of that pixel, which can be expressed as:

$$\Psi(u, v) = [\phi_1, \phi_2, \dots, \phi_d, \dots, \phi_D], \quad (1)$$

where

$$\phi_d = \begin{cases} 1 & \text{if } d = z', \\ 0 & \text{if } d \neq z'. \end{cases} \quad (2)$$

By applying Eq. 1 to each pixel in the depth map, we can obtain the depth one-hot encoding of the entire map, denoted as Ψ . This representation is sensitive to depth variations, aiding in distinguishing different objects. However, it heavily depends on the accuracy of the depth map. Moreover, this method generates a narrow response on the surface of the 3D object, limiting its ability to fully capture the three-dimensional structure.

Depth Distribution. Similar to depth one-hot encoding representation, the depth distribution of a pixel in the depth map can be represented as follows:

$$P = [p_1, p_2, \dots, p_d, \dots, p_D], \quad (3)$$

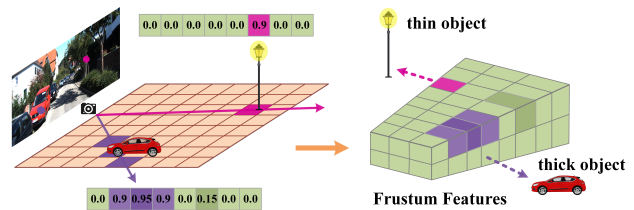


Figure 4. Thickness indicated by Depth Thickness Field along the camera ray.

where p_d represents the probability that the depth value z' lies within the d -th depth bin, satisfying the following constraint:

$$\sum_{d=1}^D p_d = 1, \quad p_d \geq 0. \quad (4)$$

Compared to depth one-hot encoding, depth distribution incorporates uncertainty when representing the depth probability distribution with depth bins, reducing the reliance on precise depth estimation. However, it still fails to fully capture the 3D structure (e.g., thickness) due to the absence of implicit thickness-aware guidance.

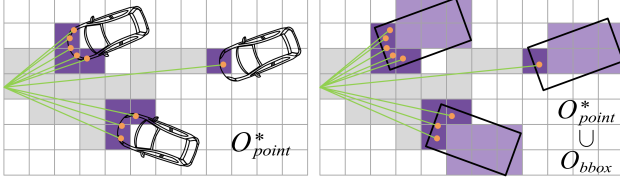
Depth Thickness Field. Unlike the two depth representations discussed above, we propose a novel depth thickness field method for mapping the given depth map. Our approach can implicitly represent the thickness of objects (as shown in Fig. 4), thereby enabling meaningful depth cues for 3D object detection. The details are as follows.

Given a pixel in a depth map, its depth thickness field F can be expressed as:

$$F = [f_1, f_2, \dots, f_d, \dots, f_D], \quad (5)$$

where $0 \leq f_d \leq 1$, represents the value of the d -th depth bin along the camera ray.

The depth thickness field is not directly derived from the depth map. Instead, it is adaptively regressed by the net-



(a) Occupancy labels obtained from OccupancyM3D [30]. (b) Occupancy labels obtained from MonoDTF (Ours).

Figure 5. An slice example of occupancy map at a certain height. (a) OccupancyM3D takes voxels containing point clouds as positive samples (dark purple) and those passed through by camera ray and without point clouds as negative samples (gray). (b) Our method enhances (a) by incorporating voxels contained within the 3D boxes as positive samples (light purple).

work. While the depth distribution is also regressed, its supervision depends on pixel-wise ground truth depth values, which results in a limited range of responses within the depth bins. In contrast, our depth thickness field regression is guided by a soft-extended depth one-hot encoding constraint (detailed in Sec. 3.3), producing a broader range of responses (as shown in Fig. 3) and enabling an adaptive representation of object thickness.

3.3. Scene-Level Depth Retargeting

These methods [30, 33] based on the LSS framework usually use depth information to explicitly transform 2D image features into 3D frustum features. However, due to the imperfect depth representation, the generated frustum features are not sufficient to perceive the 3D structure, resulting in inaccurate detection results. To address the challenges, we design the Scene-Level Depth Retargeting (SDR) module to retarget the traditional depth representations to the depth thickness field, thereby obtaining more meaningful frustum features for the subsequent 3D detection procedure. Specifically, given an RGB image $\mathbf{I} \in \mathbb{R}^{W_I \times H_I \times 3}$ and its corresponding depth map $\mathbf{D} \in \mathbb{R}^{W_I \times H_I}$, we first use a pre-trained backbone to extract image features $\mathbf{F} \in \mathbb{R}^{W_F \times H_F \times C}$. Simultaneously, we downsample the depth map and apply the LID method to produce D depth bins for each pixel in the depth map. Subsequently, we employ Eq. 1 to obtain the depth one-hot encoding representation $\Psi \in \mathbb{R}^{W_F \times H_F \times D}$ of the depth map.

Given a pixel located at the position (u, v) in the feature map, we can get the corresponding frustum feature grid $\mathbf{G}(u, v)$ as follows:

$$\mathbf{G}(u, v) = \Psi(u, v) \otimes \mathbf{F}(u, v), \quad (6)$$

where $\mathbf{G}(u, v) \in \mathbb{R}^{D \times C}$; \otimes indicates the outer products. Applying Eq. 6 to each pixel in the feature map, we can get the whole frustum features $\mathbf{G} \in \mathbb{R}^{W_F \times H_F \times D \times C}$. Then we use three 3D convolution layers followed by a sigmoid

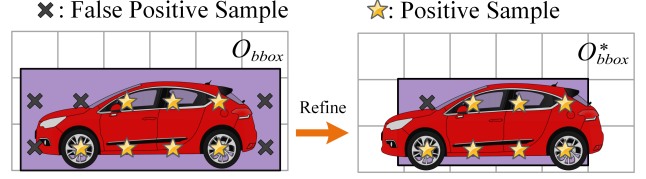


Figure 6. An slice example of occupancy map. Refining the 3D bounding box can reduce the False Positive Occupancy, thereby alleviating the ambiguity in the occupancy map.

function to refine the frustum features and regress the depth thickness field $\mathbf{D}^{thickness} \in \mathbb{R}^{W_F \times H_F \times D}$. Finally, we can produce meaningful and progressive frustum features $\tilde{\mathbf{G}}$ as follows:

$$\tilde{\mathbf{G}} = \mathbf{D}^{thickness} \otimes \mathbf{F}, \quad (7)$$

where $\tilde{\mathbf{G}} \in \mathbb{R}^{W_F \times H_F \times D \times C}$.

As previously mentioned, the depth thickness field is adaptively generated by the network. To ensure the DTF accurately reflects object thickness, we impose the following constraints. Firstly, we define a mask to extend the response range within the standard depth one-hot encoding:

$$M = [m_1, m_2, \dots, m_d, \dots, m_D], \quad (8)$$

where

$$m_d = \begin{cases} 1 & |d - z'| > l \text{ or } d = z', \\ 0 & \text{else.} \end{cases} \quad (9)$$

where l represents the extended response range; z' has been defined in Sec. 3.2. Then the soft-extended depth one-hot encoding $\tilde{\Psi}(u, v)$ of a pixel in the depth map can be denoted as follows:

$$\tilde{\Psi}(u, v) = \Psi(u, v) \odot M, \quad (10)$$

where \odot indicates the element-wise products. Finally, we introduce the focal loss [22] to formulate the objective function of this part as follows:

$$L_{thickness} = \frac{1}{W_F \cdot H_F} FL(\tilde{\Psi}, \mathbf{D}^{thickness}). \quad (11)$$

3.4. Instance-Level Spatial Refinement

OccupancyM3D [30] enhances 3D spatial features by learning an occupancy representation in voxel space. However, the labels used to guide the occupancy representation generation emanate from sparse point clouds, which are confined to the object's surface (as shown in Fig. 5a). As a result, they fail to accurately capture the thickness along the camera ray. Additionally, the limited perception range of LiDAR further restricts the ability to impose effective constraints on distant objects, exacerbating the ill-posed problem in the labels. This limitation significantly impacts the

Method	Reference	$Test, AP_{3D} R_{40}$			$Test, AP_{BEV} R_{40}$			$Val, AP_{3D} R_{40}$		
		Easy	Moderate	Hard	Easy	Moderate	Hard	Easy	Moderate	Hard
MonoDTR [10]	CVPR22	21.99	15.39	12.73	28.59	20.38	17.14	28.84	20.61	16.38
DEVIANT [15]	ECCV22	21.88	14.46	11.89	29.65	20.44	17.43	24.63	16.54	14.52
DID-M3D [29]	ECCV22	24.40	16.29	13.75	32.95	22.76	19.83	22.98	16.12	14.03
MonoDDE [18]	CVPR22	24.93	17.14	15.10	33.58	23.46	20.37	26.66	19.75	16.72
MonoNeRD [42]	ICCV23	22.75	17.13	15.63	31.13	23.46	20.97	22.03	15.44	13.99
MonoDETR [48]	ICCV23	25.00	16.47	13.58	33.60	22.11	18.60	28.84	20.61	16.38
MonoUNI [13]	NeurIPS23	24.75	16.73	13.49	33.28	23.05	19.39	24.51	17.18	14.01
MonoATT [49]	CVPR23	24.72	17.37	15.00	36.87	24.42	21.88	29.01	23.49	19.60
FD3D [41]	AAAI24	26.35	18.72	15.97	34.20	23.72	20.76	28.22	20.23	17.04
MonoLSS [20]	3DV24	26.11	19.15	16.94	34.89	25.95	22.59	25.91	18.29	15.94
MonoCD [43]	CVPR24	25.53	16.59	14.53	33.41	22.81	19.57	26.45	19.37	16.38
MonoDiff [32]	CVPR24	30.18	21.02	18.16	-	-	-	32.18	22.02	19.84
OccupancyM3D [30]	CVPR24	25.55	17.02	14.79	35.38	24.18	21.37	26.87	19.96	17.15
MonoMAE [12]	NeurIPS24	25.60	18.84	16.78	34.15	24.93	21.76	30.29	20.90	17.61
MonoDTF(Ours)	-	32.02	21.19	18.80	42.67	28.92	25.89	36.17	26.76	23.67
<i>Improvement</i>	<i>v.s. second-best</i>	+1.84	+0.17	+0.64	+5.80	+2.97	+3.3	+3.99	+3.27	+3.83

Table 1. Comparisons on KITTI *test* and *val* sets for Car category. Results are shown using the $AP(IoU = 0.7)|R_{40}$ metric. We indicate the highest result with **red** and the second highest with **blue**. The performance metrics for the other methods are reported from the respective published results.

network’s performance. To address this challenge, we design the Instance-Level Spatial Refinement (ISR) module to refine the voxel spatial representation with the guidance of instances.

Given voxel features $\mathbf{V} \in \mathbb{R}^{X \times Y \times Z \times C}$, we use 3D convolution with a sigmoid function to obtain the voxel occupancy features $\mathbf{O} \in \mathbb{R}^{X \times Y \times Z \times 1}$ which then are employed to refine the previous voxel features. This procedure can be expressed as follows:

$$\begin{aligned} \mathbf{O} &= \text{Sigmoid}(f(\mathbf{V})), \\ \tilde{\mathbf{V}} &= \mathbf{O} \odot \mathbf{V}, \end{aligned} \quad (12)$$

where $f(\cdot)$ denotes a 3D hourglass-like design [2] and \odot denotes the element-wise products.

Occupancy Labels. To generate more complete and precise occupancy labels for 3D object detection, we propose leveraging 3D bounding boxes to assist sparse point clouds in representing object thickness. Firstly, similar to OccupancyM3D [30], we denote the 3D occupancy labels derived from sparse point clouds as $O_{point}^* \in \mathbb{R}^{X \times Y \times Z}$, where X , Y , and Z are determined by the predefined voxel size and detection range, as illustrated in Figure 5a. Then we denote an additional 3D occupancy label derived from 3D bounding boxes as $O_{bbox} \in \mathbb{R}^{X \times Y \times Z}$ to complement O_{point}^* , as shown in Figure 5b.

Considering that the ISR module learns the occupancy representation within the voxel space and that the original 3D bounding boxes do not precisely conform to the object’s shape, directly using them would result in ambiguous occupancy labels. To address this issue, we propose constructing refined 3D bounding boxes, derived from the originals, as shown in Fig. 6. These adjusted boxes retain the same

center but are scaled down to reduce ambiguity in the occupancy labels. Specifically, let $\tilde{\mathbf{B}} \in \mathbb{R}^{N \times 7}$ represent the refined 3D bounding boxes. For each voxel block within the voxel space, if it falls within any of the 3D bounding boxes, we designate it as occupied. Using this approach, we obtain additional 3D occupancy labels $O_{bbox}^* \in \mathbb{R}^{X \times Y \times Z}$ derived from the 3D bounding boxes. The final occupancy label is then obtained by taking the union of O_{point}^* and O_{bbox}^* , i.e., $O^* = O_{point}^* \cup O_{bbox}^*$.

The ISR module enhances the perception of instances by adding occupancy labels from the 3D bounding boxes and then using it to refine the voxel spatial representation, which is beneficial in improving detection accuracy.

3.5. Loss Function

Our objective function consists of three components: the first for 3D object detection, the second for learning occupancy in 3D voxel space, and the third for learning the depth thickness field. The first component follows the approach of CaDDN [33], denoted as \mathcal{L}_{org} . For the occupancy component, we adopt the loss function from OccupancyM3D [30], represented as \mathcal{L}_{occ} . The third component involves the depth thickness field, for which we use the thickness loss $\mathcal{L}_{thickness}$, as defined in Section 3.3. The overall objective function is then formulated as follows:

$$\mathcal{L} = \mathcal{L}_{org} + \mathcal{L}_{occ} + \mathcal{L}_{thickness} \quad (13)$$

4. Experiments

4.1. Implementation Details

We employ PyTorch [28] for implementation. The network is trained on 3 NVIDIA 4090 (24G) GPUs. We use Adam

Method	Reference	$3DmAP/mAPH(IoU = 0.7)$				$3DmAP/mAPH(IoU = 0.5)$			
		Overall	0 - 30m	30 - 50m	50m - ∞	Overall	0 - 30m	30 - 50m	50m - ∞
LEVEL 1									
DEVIANT [15]	ECCV22	2.69/2.67	6.95/6.90	0.99/0.98	0.02/0.02	10.98/10.89	26.85/26.64	5.13/5.08	0.18/0.18
DID-M3D [29]	ECCV22	-/-	-/-	-/-	-/-	20.66/20.47	40.92/40.60	15.63/15.48	5.35/5.24
MonoNeRD [42]	ICCV23	10.66/10.56	27.84/27.57	5.40/5.36	0.72/0.71	31.18/30.70	61.11/60.28	26.08/25.71	6.60/6.47
MonoUNI [13]	NeurIPS23	3.20/3.16	8.61/8.50	0.87/0.86	0.13/0.12	10.98/10.73	26.63/26.30	4.04/3.98	0.57/0.55
MonoLSS [20]	3DV24	3.71/3.69	9.82/9.75	1.14/1.13	0.16/0.16	13.49/13.38	33.64/33.39	6.45/6.40	1.29/1.26
MonoDiff [32]	CVPR24	-/-	-/-	-/-	-/-	32.28/31.49	63.94/62.13	25.91/25.47	7.51/7.34
OccupancyM3D [30]	CVPR24	10.61/10.53	29.18/28.96	4.49/4.46	0.41/0.40	28.99/28.66	61.24/60.63	23.25/23.00	3.65/3.59
MonoDTF(Ours)	-	18.04/17.79	47.57/46.96	9.09/9.00	0.64/0.63	42.06/41.24	80.81/79.46	40.42/39.81	6.41/6.21
LEVEL 2									
DEVIANT [15]	ECCV22	2.52/2.50	6.93/6.87	0.95/0.94	0.02/0.02	10.29/10.20	26.75/26.54	4.95/4.90	0.16/0.16
DID-M3D [29]	ECCV22	-/-	-/-	-/-	-/-	19.37/19.19	40.77/40.46	15.18/15.04	4.69/4.59
MonoNeRD [42]	ICCV23	10.03/9.93	27.75/27.48	5.25/5.21	0.60/0.59	29.29/28.84	60.91/60.08	25.36/25.00	5.77/5.66
MonoUNI [13]	NeurIPS23	3.04/3.00	8.59/8.48	0.85/0.84	0.12/0.12	10.38/10.24	26.57/26.24	3.95/3.89	0.53/0.51
MonoLSS [20]	3DV24	3.27/3.25	9.79/9.73	1.11/1.10	0.15/0.15	13.12/13.02	33.56/33.32	6.28/6.22	1.15/1.13
MonoDiff [32]	CVPR24	-/-	-/-	-/-	-/-	30.73/30.48	63.86/62.92	25.28/24.86	6.43/6.29
OccupancyM3D [30]	CVPR24	10.02/9.94	28.38/28.17	4.38/4.34	0.36/0.36	27.21/26.90	61.09/60.49	22.59/22.34	3.18/3.13
MonoDTF(Ours)	-	16.77/16.54	46.94/46.34	8.76/8.67	0.55/0.54	39.20/38.44	79.93/78.60	39.04/38.45	5.56/5.39

Table 2. Comparisons on Waymo *val* set for *Vehicle* category. We indicate the highest result with **red** and the second highest with **blue**. The performance metrics for the other methods are reported from the respective published results.

Exp.	SDR	ISR	$Test, AP_{3D} R_{40}/AP_{BEV} R_{40}$			$Val, AP_{3D} R_{40}/AP_{BEV} R_{40}$		
			Easy	Moderate	Hard	Easy	Moderate	Hard
(a)			26.95/37.64	16.15/23.26	13.45/19.77	28.15/41.71	21.62/31.53	19.11/28.34
(b)	✓		31.12/40.76	20.04/27.49	17.33/24.29	36.71/51.60	25.52/35.12	22.17/31.83
(c)		✓	31.97/42.29	19.79/27.28	17.38/24.27	35.67/48.06	24.96/33.60	21.50/29.49
(d)	✓	✓	32.02/42.67	21.19/28.92	18.80/25.92	36.17/47.42	26.76/35.68	23.67/31.94

Table 3. Main ablations on KITTI *test* and *val* sets. ‘‘Exp.’’ means experiment; ‘‘SDR’’ refers to Scene-Level Depth Retargeting module; ‘‘ISR’’ denotes Instance-Level Spatial Refinement module.

[14] optimizer with an initial learning rate of 0.001 and employ the one-cycle learning rate policy [36]. On KITTI dataset [7], we train the model for 80 epochs with a total batch size of 12 and use $[2, 46.8] \times [-30.08, 30.08] \times [-3, 1]$ (meter) for the range of BEV space. On Waymo dataset [6], we downsample the input size to 640×960 and train 12 epochs with a detection range $[2, 59.6] \times [-25.6, 25.6] \times [-2, 2]$ (meter). The voxel size for the KITTI and Waymo datasets is $[0.16, 0.16, 0.16]$ (meter).

4.2. Benchmarks and Metrics

KITTI. KITTI is the most widely used benchmark [7] for 3D object detection, consisting of 7,481 training samples and 7,518 testing samples. Only annotations of the training set are made public. The training set is commonly divided into KITTI *train* with 3712 samples and KITTI *val* with 3769 samples following [3]. There are three difficulty levels, easy, moderate, and hard, defined by bounding box height and occlusion level. Following common practice, we use $AP_{3D}|R_{40}$ and $AP_{BEV}|R_{40}$ under *IoU* threshold of 0.7 to evaluate the performance.

Waymo. The Waymo Open Dataset [6] is a large dataset that contains 798 sequences for training and 202 sequences for validation. Following previous works [30, 33], we report the performance on Waymo *val* set for the vehicle category using samples only from the front camera. Results on Waymo *val* are measured by official evaluation of the mean average precision (mAP) and the mean average precision weighted by heading (mAPH).

4.3. Main Results

KITTI. Table 1 shows the main results of MonoDTF on KITTI test and val sets. Our method achieves the best results under three-level difficulty settings in AP_{BEV} and AP_{3D} . On the test set, MonoDTF exceeds all existing methods and surpasses the second-best under three-level difficulties by $+1.84/+0.17/+0.64$ in AP_{3D} , and by $+7.29/+2.97/+3.33$ in AP_{BEV} . In particular, MonoDTF does not require the depth ground truth (GT) that is hard to obtain for supervision when training the detection model. Guided by accurate depth priors, our method transforms tra-

Exp.	Depth Model	SDR&ISR	$T_{est}, AP_{3D} R_{40}/AP_{BEV} R_{40}$			$Val, AP_{3D} R_{40}/AP_{BEV} R_{40}$		
			Easy	Moderate	Hard	Easy	Moderate	Hard
(1)	MonoDepth2* [8]		20.41/28.33	12.03/17.45	10.30/14.89	20.39/31.34	14.90/22.56	12.42/19.05
(2)	MonoDepth2*	✓	21.65/29.71	14.13/19.42	11.73/16.99	22.01/31.57	16.54/23.62	14.17/20.46
Improvement			+1.24/+1.38	+2.1/+1.97	+1.43/+2.1	+1.62/+0.23	+1.64/+1.06	+1.75/+1.41
(3)	DAMv2† [45]		26.90/38.51	15.40/22.86	12.48/19.26	35.24/48.36	20.97/29.94	17.09/24.65
(4)	DAMv2†	✓	32.74/41.72	20.19/27.11	17.04/23.36	39.82/52.30	27.46/37.79	24.12/33.74
Improvement			+5.84/+3.21	+4.79/+4.25	+4.56/+4.10	+4.58/+3.94	+6.49/+7.85	+7.03/+9.09
(5)	Metric3Dv2 [46]		26.95/37.64	16.15/23.26	13.45/19.77	28.15/41.71	21.62/31.53	19.11/28.34
(6)	Metric3Dv2	✓	32.02/42.67	21.19/28.92	18.80/25.89	36.17/47.42	26.76/35.68	23.67/31.94
Improvement			+5.25/+5.03	+5.04/+5.66	+5.35/+6.12	+8.02/+5.71	+5.14/+4.15	+4.56/+3.60

Table 4. Ablations of different depth estimation models on KITTI *test* and *val* sets. * denotes the lightweight model and † indicates the further fine-tuned model. “DAMv2” refers to Depth Anything V2 [45].

Exp.	Representation	$T_{est}, AP_{3D} R_{40}/AP_{BEV} R_{40}$		
		Easy	Moderate	Hard
1)	One-Hot	26.95/37.64	16.15/23.26	13.45/19.77
2)	Distribution	30.37/40.42	19.16/26.69	17.02/24.12
3)	Thickness	32.02/42.67	21.19/28.92	18.80/25.89

Table 5. Ablation of depth representation. One-Hot: Depth One-Hot Encoding; Distribution: Depth Distribution; Thickness: Depth Thickness Field.

ditional depth representations into a more effective depth thickness field for 3D detection, resulting in a significant improvement over existing approaches.

Waymo. We also evaluate our method on Waymo Open Dataset (Waymo) [6]. As shown in Table 2, our method obtains promising results, significantly outperforming existing methods in “0-30m”, “30-50m”, and “Overall”. For example, under LEVEL 1 setting, MonoDTF outperforms the second best by +7.38/+7.23 and +9.78/+9.75 (mAP/mAPH) with IoU 0.7 and 0.5 criteria respectively; under LEVEL 2 setting, MonoDTF outperforms the second best by +6.74/+6.60 and +8.47/+7.96 (mAP/mAPH) with IoU 0.7 and 0.5 criteria respectively. This success can be attributed to the effective depth thickness field representation. For objects within [50m, ∞], our method performs relatively worse. This is because our method is BEV-based, which has a detection range limitation: [2, 59.6] (*meters*).

4.4. Ablations

To illustrate the effectiveness of SDR and ISR modules proposed in this paper, we carry out ablations on both KITTI *test* and *val* sets as shown in Table 3. **SDR:** Exp. (a) is the baseline which directly uses depth one-hot encoding to generate 3D features for 3D object detection. In Exp. (b), when retargeting depth representation from depth one-hot encoding to depth thickness field, the detection AP_{3D} increases from 26.95/16.15/13.45 to 31.12/20.04/17.33 on the *test* set.

ISR: As shown in Exp. (c), when enforcing the refinement of voxel spatial representation via learning 3D occupation with the guidance of instances, the detection AP_{3D} is boosted to 31.97/19.79/17.38 on the *test* set. Finally, we can see that MonoDTF obtains +5.25/+5.04/+5.35 in AP_{3D} compared to the baseline of Exp. (d).

Universality Analysis. In Table 4, we report the performance of MonoDTF when equipped with different depth estimation models. DAMv2 and Metric3Dv2 are large models used for depth estimation, distinguished by their methodology. DAMv2 initially produces relative depth, which requires fine-tuning of the metric depth data for 3D detection. In contrast, Metric3Dv2 provides metric depth directly, obviating the requirement for fine-tuning. The results indicate significant improvements in detection performance when integrated with our method. As an early lightweight model for depth estimation, MonoDepth2 still benefits from our method for monocular 3D object detection. These experiments demonstrate both the effectiveness and the universality of MonoDTF.

Ablations on Depth Representations. In Table 5, we report the performances when replacing the depth thickness field with traditional depth representations (*e.g.*, depth one-hot encoding and depth distribution). We can observe that the depth thickness field performs better than the traditional depth representations.

5. Conclusion

In this paper, we propose a depth-adapted network for monocular 3D object detection. Unlike current approaches, we reformulate a new key factor of the depth-assisted method from depth accuracy to the adaptability of depth representation and introduce a novel depth representation. The proposed SDR module retargets traditional depth representations to depth thickness field with self-supervision. We also introduce the ISR module to refine the voxel spatial representation with the guidance of instances. We

conduct experiments on the challenging KITTI and Waymo open datasets. The results demonstrate our superiority to existing state-of-the-art (SoTA) methods and the universality when equipped with different depth estimation models.

References

- [1] Johann Cabon, Naila Murray, and Martin Humenberger. Virtual kitti 2. *arXiv preprint arXiv:2001.10773*, 2020. **2**
- [2] Jia-Ren Chang and Yong-Sheng Chen. Pyramid stereo matching network. In *Proceedings of the IEEE conference on computer vision and pattern recognition*, pages 5410–5418, 2018. **6**
- [3] Xiaozhi Chen, Kaustav Kundu, Yukun Zhu, Huimin Ma, Sanja Fidler, and Raquel Urtasun. 3d object proposals using stereo imagery for accurate object class detection. *IEEE transactions on pattern analysis and machine intelligence*, 40(5):1259–1272, 2017. **7**
- [4] Zhiyu Chong, Xinzhu Ma, Hong Zhang, Yuxin Yue, Haojie Li, Zhihui Wang, and Wanli Ouyang. Monodistill: Learning spatial features for monocular 3d object detection. *arXiv preprint arXiv:2201.10830*, 2022. **1**
- [5] Mingyu Ding, Yuqi Huo, Hongwei Yi, Zhe Wang, Jianping Shi, Zhiwu Lu, and Ping Luo. Learning depth-guided convolutions for monocular 3d object detection. In *Proceedings of the IEEE/CVF Conference on computer vision and pattern recognition workshops*, pages 1000–1001, 2020. **1**
- [6] Scott Ettinger, Shuyang Cheng, Benjamin Caine, Chenxi Liu, Hang Zhao, Sabeek Pradhan, Yuning Chai, Ben Sapp, Charles R Qi, Yin Zhou, et al. Large scale interactive motion forecasting for autonomous driving: The waymo open motion dataset. In *Proceedings of the IEEE/CVF International Conference on Computer Vision*, pages 9710–9719, 2021. **7, 8**
- [7] Andreas Geiger, Philip Lenz, and Raquel Urtasun. Are we ready for autonomous driving? the kitti vision benchmark suite. In *2012 IEEE conference on computer vision and pattern recognition*, pages 3354–3361. IEEE, 2012. **7**
- [8] Clément Godard, Oisín Mac Aodha, Michael Firman, and Gabriel J Brostow. Digging into self-supervised monocular depth estimation. In *Proceedings of the IEEE/CVF international conference on computer vision*, pages 3828–3838, 2019. **2, 8**
- [9] Junjie Huang, Guan Huang, Zheng Zhu, Yun Ye, and Dalong Du. Bevdet: High-performance multi-camera 3d object detection in bird-eye-view. *arXiv preprint arXiv:2112.11790*, 2021. **1, 2**
- [10] Kuan-Chih Huang, Tsung-Han Wu, Hung-Ting Su, and Winston H Hsu. Monodrtr: Monocular 3d object detection with depth-aware transformer. In *Proceedings of the IEEE/CVF conference on computer vision and pattern recognition*, pages 4012–4021, 2022. **2, 6**
- [11] Yuanhui Huang, Wenzhao Zheng, Yunpeng Zhang, Jie Zhou, and Jiwen Lu. Tri-perspective view for vision-based 3d semantic occupancy prediction. In *Proceedings of the IEEE/CVF conference on computer vision and pattern recognition*, pages 9223–9232, 2023. **3**
- [12] Xueying Jiang, Sheng Jin, Xiaoqin Zhang, Ling Shao, and Shijian Lu. Monomae: Enhancing monocular 3d detection through depth-aware masked autoencoders. *arXiv preprint arXiv:2405.07696*, 2024. **6**
- [13] Jia Jinrang, Zhenjia Li, and Yifeng Shi. Monouni: A unified vehicle and infrastructure-side monocular 3d object detection network with sufficient depth clues. *Advances in Neural Information Processing Systems*, 36:11703–11715, 2023. **6, 7**
- [14] Diederik P Kingma. Adam: A method for stochastic optimization. *arXiv preprint arXiv:1412.6980*, 2014. **7**
- [15] Abhinav Kumar, Garrick Brazil, Enrique Corona, Armin Parchami, and Xiaoming Liu. Deviant: Depth equivariant network for monocular 3d object detection. In *European Conference on Computer Vision*, pages 664–683. Springer, 2022. **6, 7**
- [16] Alex H Lang, Sourabh Vora, Holger Caesar, Lubing Zhou, Jiong Yang, and Oscar Beijbom. Pointpillars: Fast encoders for object detection from point clouds. In *Proceedings of the IEEE/CVF conference on computer vision and pattern recognition*, pages 12697–12705, 2019. **1**
- [17] Yin hao Li, Zheng Ge, Guanyi Yu, Jinrong Yang, Zengran Wang, Yukang Shi, Jianjian Sun, and Zeming Li. Bevdepth: Acquisition of reliable depth for multi-view 3d object detection. In *Proceedings of the AAAI Conference on Artificial Intelligence*, pages 1477–1485, 2023. **1, 2, 3**
- [18] Zhuoling Li, Zhan Qu, Yang Zhou, Jianzhuang Liu, Haoqian Wang, and Lihui Jiang. Diversity matters: Fully exploiting depth clues for reliable monocular 3d object detection. In *Proceedings of the IEEE/CVF Conference on Computer Vision and Pattern Recognition*, pages 2791–2800, 2022. **6**
- [19] Zhiqi Li, Wenhao Wang, Hongyang Li, Enze Xie, Chonghao Sima, Tong Lu, Yu Qiao, and Jifeng Dai. Bevformer: Learning bird’s-eye-view representation from multi-camera images via spatiotemporal transformers. In *European conference on computer vision*, pages 1–18. Springer, 2022. **1, 2**
- [20] Zhenjia Li, Jinrang Jia, and Yifeng Shi. Monolss: Learnable sample selection for monocular 3d detection. In *2024 International Conference on 3D Vision (3DV)*, pages 1125–1135. IEEE, 2024. **2, 6, 7**
- [21] Pan Liao, Feng Yang, Di Wu, and Liu Bo. Monodetrnext: Next-generation accurate and efficient monocular 3d object detection method. *arXiv preprint arXiv:2405.15176*, 2024. **1**
- [22] T Lin. Focal loss for dense object detection. *arXiv preprint arXiv:1708.02002*, 2017. **5**
- [23] Hou-I Liu, Christine Wu, Jen-Hao Cheng, Wenhao Chai, Shian-Yun Wang, Gaowen Liu, Jenq-Neng Hwang, Hong-Han Shuai, and Wen-Huang Cheng. Monotakd: Teaching assistant knowledge distillation for monocular 3d object detection. *arXiv preprint arXiv:2404.04910*, 2024. **1**
- [24] Zhijian Liu, Haotian Tang, Alexander Amini, Xinyu Yang, Huizi Mao, Daniela L Rus, and Song Han. Bevfusion: Multi-task multi-sensor fusion with unified bird’s-eye view representation. In *2023 IEEE international conference on robotics and automation (ICRA)*, pages 2774–2781. IEEE, 2023. **2**

- [25] Yan Lu, Xinzhu Ma, Lei Yang, Tianzhu Zhang, Yating Liu, Qi Chu, Junjie Yan, and Wanli Ouyang. Geometry uncertainty projection network for monocular 3d object detection. In *Proceedings of the IEEE/CVF International Conference on Computer Vision*, pages 3111–3121, 2021. [2](#)
- [26] Xinzhu Ma, Wanli Ouyang, Andrea Simonelli, and Elisa Ricci. 3d object detection from images for autonomous driving: a survey. *IEEE Transactions on Pattern Analysis and Machine Intelligence*, 46(5):3537–3556, 2023. [1](#), [3](#)
- [27] Dennis Park, Rares Ambrus, Vitor Guizilini, Jie Li, and Adrien Gaidon. Is pseudo-lidar needed for monocular 3d object detection? In *Proceedings of the IEEE/CVF International Conference on Computer Vision*, pages 3142–3152, 2021. [2](#)
- [28] Adam Paszke, Sam Gross, Francisco Massa, Adam Lerer, James Bradbury, Gregory Chanan, Trevor Killeen, Zeming Lin, Natalia Gimelshein, Luca Antiga, et al. Pytorch: An imperative style, high-performance deep learning library. *Advances in neural information processing systems*, 32, 2019. [6](#)
- [29] Liang Peng, Xiaopei Wu, Zheng Yang, Haifeng Liu, and Deng Cai. Did-m3d: Decoupling instance depth for monocular 3d object detection. In *European Conference on Computer Vision*, pages 71–88. Springer, 2022. [1](#), [2](#), [4](#), [6](#), [7](#)
- [30] Liang Peng, Junkai Xu, Haoran Cheng, Zheng Yang, Xiaopei Wu, Wei Qian, Wenxiao Wang, Boxi Wu, and Deng Cai. Learning occupancy for monocular 3d object detection. In *Proceedings of the IEEE/CVF Conference on Computer Vision and Pattern Recognition*, pages 10281–10292, 2024. [1](#), [2](#), [5](#), [6](#), [7](#)
- [31] Jonah Philion and Sanja Fidler. Lift, splat, shoot: Encoding images from arbitrary camera rigs by implicitly unprojecting to 3d. In *Computer Vision—ECCV 2020: 16th European Conference, Glasgow, UK, August 23–28, 2020, Proceedings, Part XIV 16*, pages 194–210. Springer, 2020. [1](#), [2](#), [3](#)
- [32] Yasiru Ranasinghe, Deepti Hegde, and Vishal M Patel. Monodiff: Monocular 3d object detection and pose estimation with diffusion models. In *Proceedings of the IEEE/CVF Conference on Computer Vision and Pattern Recognition*, pages 10659–10670, 2024. [6](#), [7](#)
- [33] Cody Reading, Ali Harakeh, Julia Chae, and Steven L Waslander. Categorical depth distribution network for monocular 3d object detection. In *Proceedings of the IEEE/CVF Conference on Computer Vision and Pattern Recognition*, pages 8555–8564, 2021. [2](#), [3](#), [5](#), [6](#), [7](#)
- [34] Zhijie Shen, Chunyu Lin, Kang Liao, Lang Nie, Zishuo Zheng, and Yao Zhao. Panoformer: Panorama transformer for indoor 360 depth estimation. In *European Conference on Computer Vision*, pages 195–211. Springer, 2022. [2](#)
- [35] Shaoshuai Shi, Chaoxu Guo, Li Jiang, Zhe Wang, Jianping Shi, Xiaogang Wang, and Hongsheng Li. Pv-rcnn: Point-voxel feature set abstraction for 3d object detection. In *Proceedings of the IEEE/CVF conference on computer vision and pattern recognition*, pages 10529–10538, 2020. [1](#)
- [36] Leslie N Smith. A disciplined approach to neural network hyper-parameters: Part 1—learning rate, batch size, momentum, and weight decay. *arXiv preprint arXiv:1803.09820*, 2018. [7](#)
- [37] Julian Straub, Thomas Whelan, Lingni Ma, Yufan Chen, Erik Wijmans, Simon Green, Jakob J Engel, Raul Mur-Artal, Carl Ren, Shobhit Verma, et al. The replica dataset: A digital replica of indoor spaces. *arXiv preprint arXiv:1906.05797*, 2019. [2](#)
- [38] Yunlei Tang, Sebastian Dorn, and Chiragkumar Savani. Center3d: Center-based monocular 3d object detection with joint depth understanding. In *DAGM German Conference on Pattern Recognition*, pages 289–302. Springer, 2020. [4](#)
- [39] Jiyuan Wang, Chunyu Lin, Lang Nie, Shujun Huang, Yao Zhao, Xing Pan, and Rui Ai. Weatherdepth: Curriculum contrastive learning for self-supervised depth estimation under adverse weather conditions. In *2024 IEEE International Conference on Robotics and Automation (ICRA)*, pages 4976–4982. IEEE, 2024. [2](#)
- [40] Yan Wang, Wei-Lun Chao, Divyansh Garg, Bharath Hariharan, Mark Campbell, and Kilian Q Weinberger. Pseudo-lidar from visual depth estimation: Bridging the gap in 3d object detection for autonomous driving. In *Proceedings of the IEEE/CVF conference on computer vision and pattern recognition*, pages 8445–8453, 2019. [1](#)
- [41] Zizhang Wu, Yuanzhu Gan, Yunzhe Wu, Ruihao Wang, Xiaoquan Wang, and Jian Pu. Fd3d: Exploiting foreground depth map for feature-supervised monocular 3d object detection. In *Proceedings of the AAAI Conference on Artificial Intelligence*, pages 6189–6197, 2024. [6](#)
- [42] Junkai Xu, Liang Peng, Haoran Cheng, Hao Li, Wei Qian, Ke Li, Wenxiao Wang, and Deng Cai. Mononerf: Nerf-like representations for monocular 3d object detection. In *Proceedings of the IEEE/CVF International Conference on Computer Vision*, pages 6814–6824, 2023. [1](#), [6](#), [7](#)
- [43] Longfei Yan, Pei Yan, Shengzhou Xiong, Xuanyu Xiang, and Yihua Tan. Monocd: Monocular 3d object detection with complementary depths. In *Proceedings of the IEEE/CVF Conference on Computer Vision and Pattern Recognition*, pages 10248–10257, 2024. [2](#), [4](#), [6](#)
- [44] Yan Yan, Yuxing Mao, and Bo Li. Second: Sparsely embedded convolutional detection. *Sensors*, 18(10):3337, 2018. [1](#)
- [45] Lihe Yang, Bingyi Kang, Zilong Huang, Zhen Zhao, Xiaogang Xu, Jiashi Feng, and Hengshuang Zhao. Depth anything v2. *arXiv preprint arXiv:2406.09414*, 2024. [2](#), [8](#)
- [46] Wei Yin, Chi Zhang, Hao Chen, Zhipeng Cai, Gang Yu, Kaixuan Wang, Xiaozhi Chen, and Chunhua Shen. Metric3d: Towards zero-shot metric 3d prediction from a single image. In *Proceedings of the IEEE/CVF International Conference on Computer Vision*, pages 9043–9053, 2023. [2](#), [8](#)
- [47] Fisher Yu, Dequan Wang, Evan Shelhamer, and Trevor Darrell. Deep layer aggregation. In *Proceedings of the IEEE conference on computer vision and pattern recognition*, pages 2403–2412, 2018. [3](#)
- [48] Renrui Zhang, Han Qiu, Tai Wang, Ziyu Guo, Ziteng Cui, Yu Qiao, Hongsheng Li, and Peng Gao. Monodetr: Depth-guided transformer for monocular 3d object detection. In *Proceedings of the IEEE/CVF International Conference on Computer Vision*, pages 9155–9166, 2023. [6](#)

- [49] Yunsong Zhou, Hongzi Zhu, Quan Liu, Shan Chang, and Minyi Guo. Monoatt: Online monocular 3d object detection with adaptive token transformer. In *Proceedings of the IEEE/CVF Conference on Computer Vision and Pattern Recognition*, pages 17493–17503, 2023. [2](#), [6](#)